Inner and outer layer turbulence over a superhydrophobic surface with low roughness level at low Reynolds number

W. Abu Rowin, J. Hou, and S. Ghaemi*
Department of Mechanical Engineering, University of Alberta, Edmonton
Alberta T6G 2G8, Canada
*ghaemi@ualberta.ca

The inner and outer layers of a turbulent channel flow over a superhydrophobic surface (SHS) is characterized using simultaneous long-range microscopic particle tracking velocimetry (micro-PTV) and particle image velocimetry (PIV), respectively. The channel flow is operated at low Reynolds number of Re_H = 4,400 (based on full channel height and 0.174 m/s bulk velocity), equivalent to Re_τ = 140 (based on half channel height and friction velocity). The SHS is produced by spray coating and the root-mean-square of wall roughness normalized by wall-unit is k^+_{rms} = 0.11. The micro-PTV shows 0.023 m/s slip velocity over the SHS (about 13% of the bulk velocity), which corresponds to a slip-length of ~200 μm. A drag reduction of ~19% based on the slope of the linear viscous sublayer and 22% based on an analytical expression of Rastegari & Akhavan [1] is realized. The reduced Re_τ over the SHS based on the corresponding friction velocity is ~125, which is in the lower limit of turbulence regime. The results shows increase of streamwise Reynolds stresses $\langle u^2 \rangle$ for the SHS in the linear viscous sublayer due to the slip boundary condition. The $\langle u^2 \rangle$ peak does not change in magnitude while it is displaced closer to the wall in physical distance. The wall-normal Reynolds stress $\langle v^2 \rangle$ over the SHS and smooth surface are observed to overlap near the wall at $y^+<10$ while $\langle v^2 \rangle$ for the SHS is smaller further away from the wall in physical dimensions. At $y^+ = 30$, $\langle v^2 \rangle$ is 30% smaller for the SHS. A small increase of Reynolds shear stress for the SHS is observed at $y^+<10$ while about 30% reduction is observed at $y^+ = 30$. The observed variation of Reynolds stresses is associated with the relatively small roughness of the surface. If Reynolds stresses are normalized based on the corresponding friction velocity, the non-dimensional stresses show a large increase of $\langle u^2 \rangle$ and a small increase of $\langle uv \rangle$ over the SHS at $y^+ < 20$. Farther away from the wall at $y^+ > 20$, the scaling of Reynolds stresses based on the corresponding u_τ results in their overlap for the smooth and SHS. The DR is mainly associated with the reduction of viscous wall-shear stress while the variation in Reynolds shear stress at the wall is negligible. The quadrant analysis of turbulent fluctuations shows attenuation of stronger sweep motions at $y^+<15$ while ejections are attenuated in the buffer layer at $y^+=20$ until 30.

I. INTRODUCTION

The combination of chemical hydrophobicity and surface texture of a superhydrophobic surface (SHS) can trap small air pockets in micro- and nano-scale pores when submerged in water [2]. The air-water interface relaxes the no-slip boundary condition by reducing the contact area between the liquid and the solid substrate. As a result, the liquid flow appears to "slip" over the superhydrophobic surface with the potential of reducing skin-friction drag [3]. Solid surfaces exhibiting slip boundary condition, if applicable in turbulent flows, can potentially reduce skin-friction drag in transportation industry. Although experiments in controlled laboratory conditions have shown up to 75% drag reduction over SHS in turbulent wall flows [4], there are still major challenges such as manufacturing large SHS and maintaining the air pockets under high pressure, high shear, and in particle-laden flows [5, 6].

In laminar micro-channels, the slip velocity is proportional to the area of the shear-free air-liquid interface [7]. Choi *et al*. [8] observed that the slip velcoity is directional by investigating surfaces with nanograting ridges (~230 nm pitch) oriented in streamiwse and tranverse direction with respect to the flow. In turbulent regime, direct numerical simulation (DNS) of Min & Kim [9] demonstrated that applying a boundary condition with streamwise slip reduces drag and turbulence, while a spanwise slip increases drag and turbulence. The experiment of Woolford *et al*. [10] also confirmed an increase of friction if superhydrophobic grooves are transverse to the flow direction. Busse & Sandham [11] showed using a DNS that drag reduction (DR) is achieved irrespective of the spanwise slip if streamwise slip is large enough. Martell *et al*. [12] modeled the slip pattern of SHSs by assuming a flat shear-free surface covered with no-slip ridges or posts in their DNS. They observed up to 40% DR and a slip velocity 75% of the bulk velocity using 30×30 μm^2 no-slip posts spaced 90 μm apart. The results agree with pressure drop measurement of Daniello *et al*. [13] showing up to 50% DR over SHS with 60 μm streamwise ridges placed 60 μm apart. In an attempt to carry out bias-free measurment, Park *et al*. [4] directly measured force over 27 × 27 mm^2 silicon chips with different streamwise groove spacing. They observed up to 75% DR over a SHS with 95% gas-fraction (the ratio of ridge area over the gap area). Jung *et al*. [14] modeled the flow inside the air layer in their DNS as a shear-driven and a recirculating flow. Their analysis shows that a thicker air-layer can increase slip velocity and DR. These investigations provide valuable insight into the morphology of patterned SHS and their DR performance. However, patterned surfaces are costly, fragile, and their production through techniques such as photolithography is still limited to small surfaces.

Superhydrophobic surfaces with random texture are typically produced by spray coating or by sand blasting, and are larger than the patterned SHS. The early experiment of Watanabe *et al*. [15] did not result in any DR in a turbulent pipe flow coated with a water-repellent layer. Aljallis *et al*. [16] observed 30% DR in transitional flows followed by drag increase in turbulent flows ($Re > 10^6$) over a flat plate coated with superhydrophobic particles. Later, Bidkar *et al*. [17] obtained up to 30% turbulent DR by direct force measurement over SHSs with random texture. Ling *et al*. [18] also observed up to 36% DR over a range of SHSs with non-porous and porous base material. The porous substrate was applied to maintain and replenish the air pockets by injecting air through the material. The loss of the air pockets/layer can occur due to instability or dissolution of air into water [5, 6] and sets a practical limitation for SHSs. It is also difficult to control and monitor the thickness and morphology of the air plastron during large-scale experiments. This has resulted in a degree of uncertainty and inconsistency when the previous experimental results are compared.

The longevity of the air layer over a SHS indicates the duration of transfer from Cassie state to Wenzel state [19, 20]. Lei *et al*. [21] observed this transfer to be reversible when a SHS with polydimethylsiloxane (PDMS) substrate is immersed in water under 50-60 mbar followed by pressure release. However, they observed permanent collapse of the air pockets due to an irreversible transfer to Wenzel state at higher pressures. Samaha *et al*. [5] used a technique based on total internal reflection of a laser beam to detect the presence of the air layer over a SHS in contact with a wall jet. Their results show that the depletion of the air layer is a function of flow rate. Vajdi Hokmabad & Ghaemi [6] also applied a similar technique to a SHS in a laminar boundary layer. They observed intensified dissolution of the plastron into the water due to convection by the flow and the presence of particulate phase. In general, the thickness and morphology of the air plastron and the DR of the SHS is a function of time, flow rate, presence of a particulate phase, and level of dissolved air.

Accurate measurement of mean velocity profile and slip velocity can characterize SHSs and guide the numerical simulations in modeling the wall boundary condition. In boundary layer flows, particle image

velocimetry (PIV) of Zhang *et al*. [22] showed a considerable increase of mean velocity $<U>$ extended up to the boundary layer edge. Woolford *et al*. [10] and Vajdi Hokmabad & Ghaemi [23] observed a negligible change in $<U>$ within the outer layer of a fully developed turbulent channel flow. Any variation of $<U>$ was conjectured to be limited to the inner layer or beyond the spatial-resolution of the PIV measurements. The theoretical work of Fukagata *et al*. [24] predicts an increase of mean velocity in the vicinity of the wall as a result of the slip and reduction of $<U>$ further away from the wall. This is consistent with DNS of Min and Kim [9] and Jelly *et al*. [25] over a surface with streamwise slip-free strips. Daniello *et al*. [13] observed slip velocity up to 0.4 m/s at Re_H = 8,200 based on PIV, although direct comparison with a baseline smooth surface and the spatial-resolution of their PIV system was not provided. Digital holographic microscopy (DHM) of Ling *et al*. [18] within the inner part of a turbulent boundary layer (y^+<200) measured slip velocity up to 0.75 m/s (~9u_τ, friction velocity) over non-porous SHSs.

To further understand the DR mechanism and obtain more detailed modeling of SHSs in turbulent flows the evaluation of turbulence statistics is needed. The standard PIV measurement of Woolford *et al*. [10] and Vajdi Hokmabad & Ghaemi [23] over SHS with 10-15% DR were limited due to their spatial-resolution to the outer layer flow. Both investigations reported reduction of streamwise $<u^2>$, wall-normal $<v^2>$, and shear Reynolds stresses $<uv>$ over their SHSs as detailed in Table 1. The DNS of Min & Kim [9] at Re_τ = 180 also shows reduction of $<u^2>$ and $<v^2>$ by prescribing the Navier slip boundary condition with resultant 17% DR. This is also in agreement with the observed reduction of all Reynolds stress components in DNS of Rastegari & Akhavan [1] at Re_τ = 223 over a SHS with 18% DR. However, the recent DHM of Ling *et al*. [18] over a variety of SHSs shows increase of Reynolds stresses in the inner layer (see Table 1) at higher Re_τ of 439 to 1389. This is particularly evident in the 42% and 92% increase of $<uv>$ over the two SHSs with 27 and 3% DR, respectively. The DR was associated with the overall reduction of viscous wall shear stress (μd$<U>$/dy) while they reported a finite Reynolds shear stress ($-\rho<uv>$) at the wall. As it is expected, the increase of $<uv>$ in the inner layer contributes to increase of wall-shear stress and has an adverse effect on the performance of SHS. Scrutiny of the surface texture of the previous experimental works shows that the surfaces investigated by Ling *et al*. [18] applied a rough surface with $0.43 \leq k^+_{rms} \leq 3.28$ (root-mean-square of roughness normalized by wall-unit) with respect to Vajdi Hokmabad & Ghaemi [23] and Woolford *et al*. [10]. However, the numerical simulations, which were carried out at lower Re_τ, assumed a flat surface and the roughness effect was not considered.

The current investigation characterizes the mean velocity profile and Reynolds stresses in both inner and outer layers of a turbulent channel flow over a SHS with an average roughness of k^+_{rms} = 0.11. The investigation characterizes the slip velocity and the effect of a surface with low roughness on Reynolds stresses at low Reynolds number of Re_τ=125 over the SHS with drag reduction. The results provide a database for evaluation of numerical simulations and the assumption of flat-boundary condition over the SHSs. Macroscopic PIV and long-range microscopic PTV (micro-PTV) are simultaneously carried out to ensure that the inner and outer layer are characterized over a common plastron morphology. The longevity of the SHS is also investigated by monitoring the variation of near-wall velocity and slip velocity using the micro-PTV over the measurement period.

Table 1 A summary of experimental and numerical investigations of Reynolds stresses in the inner and outer layer of wall flows over SHSs. The investigation method, slip velocity, root-mean-square of surface roughness normalized with wall unit (k^+_{rms}), and DR percentage is also provided. The variation of dimensional Reynolds stresses (or non-dimensional with inner scaling of the smooth wall) is reported. Only DNS of turbulent flows with constant flow rate are reported here for comparison with experiments. DNS of Martell et al. [12] and Türk et al. [26] are carried out at constant pressure drop (variable flow rate) along the channel.

Reference	Method	Re_τ	U_s	k^+_{rms}	DR %	Inner layer at y^+=10			Outer layer at y^+=50		
						$\Delta\langle u^{2+}\rangle$	$\Delta\langle v^{2+}\rangle$	$\Delta\langle uv^+\rangle$	$\Delta\langle u^{2+}\rangle$	$\Delta\langle v^{2+}\rangle$	$\Delta\langle uv^+\rangle$
Woolford *et al*. [10]	PIV	235	-	0.39	11	-	-	-	-12%[a]	-3%[a]	-12%[a]
Vajdi Hokmabad & Ghaemi [23]	PIV	246	-	0.11	15	-	-	-	-8%	-18%	-12%
Min & Kim [9]	DNS	180	$3.2u_\tau$	-	17	-21%	-29%	-	-19%	-29%	-
Rastegari & Akhavan [1]	DNS	223	$0.15U_b$	-	18	-17%	-20%	-42%	-12%	-17%	-20%
Ling *et al*. [18]	DHM	739	$0.29U_b$	0.89	27	~0	5%	42%	-17%	-3%	-7%
		1389	$0.33U_b$	1.71	3	5%	61%	92%	5%	-2%	7%
Current study	PIV PTV	140	$0.19U_b$	0.11	20	2%	~0	~0	~0	-6%	-9%

[a] Values are estimated at $y/H = 0.2$.

II.EXERIMENTAL SETUP

This section details the fully developed turbulent channel flow, the superhydrophobic surface, PIV setup for full-channel characterization, and long-range micro-PTV for characterization of the inner layer. The morphology and the volume of the air pockets over the SHS depend on the surface pattern/roughness and also the water flume condition such as dissolved oxygen, pH, temperature, and tracer concentration [6]. The latter parameters are difficult to accurately control in a large-scale experiment. Therefore, the PIV and micro-PTV measurements are simultaneously carried out to allow scrutiny of the inner and outer layer flows over the same superhydrophobic plastron.

A. Flow setup

The experiments are carried out in a turbulent channel flow with 3 m length (L) in the streamwise direction (x) and a rectangular cross-section of 25 mm (H) in the wall-normal direction (y) and 540 mm (W) in the spanwise direction (z). The channel is submerged in a flume with test section dimensions of 5.2 m long, 0.68 m wide, and 0.47 m deep as shown in Fig.1. The bottom wall of the submerged channel is a large glass sheet placed 5 cm above the bottom wall of the flume to avoid entrance of the flume boundary layer. A honeycomb flow straightener was placed at the entrance of the submerged channel as shown in Fig. 1. The side of the embedded channel has a small viewing window to provide optical access for PIV and micro-PTV cameras. The top wall is made from acrylic sheets with 1 inch thickness to accommodate a flush-mounted insert plate for testing the SHS. The insert plate is machined from an acrylic sheet (baseline surface) and is located 1.9 m (76H) downstream of the entrance and is 570 mm (22.8H) long and 320 mm wide. The long flow development length (85H till PTV measurement location) and the large aspect ratio (W/H = 21.6) ensure a fully developed turbulent channel flow at the measurement location. The flume is seeded with polyamide tracers (VESTOSINT 2070) with density of 1.016 g/cm^3 and average diameter of 5 μm. The neutrally buoyant particles are selected to minimize their impact with the surface and increase the longevity of the air pockets over the SHS [6]. The instantaneous velocity in the streamwise and wall normal

directions are indicated by U and V, respectively. The ensemble averaged quantities are specified by < > while streamwise and wall-normal velocity fluctuations are shown by u and v, respectively.

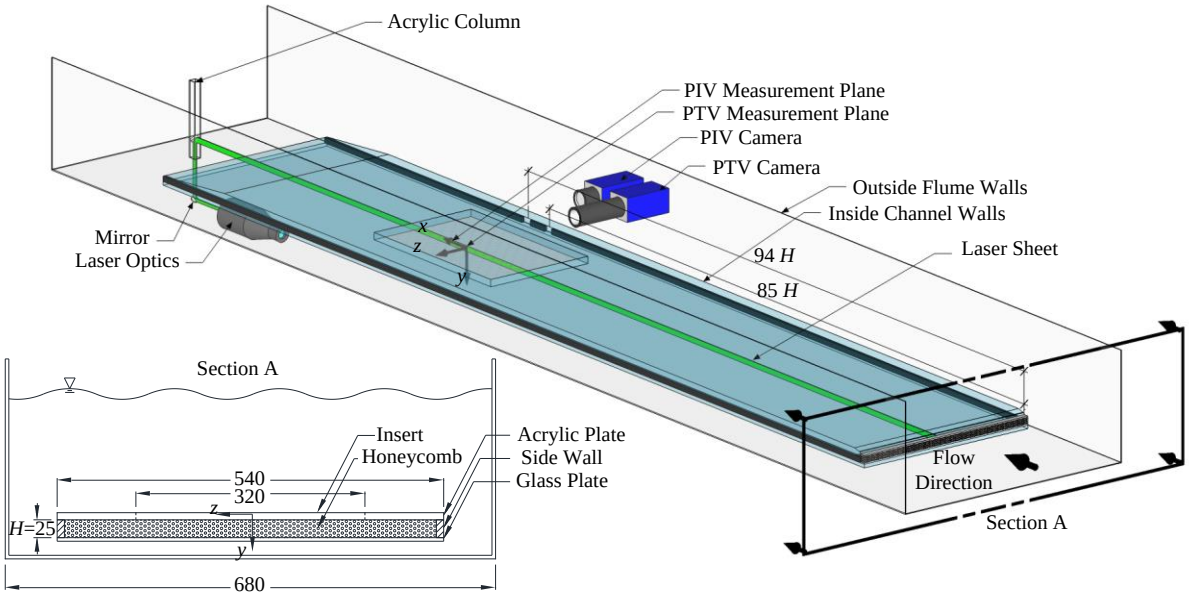

Figure 1 The experimental setup showing the channel flow consisting of a glass bottom wall, a top acrylic wall, honeycomb at the entrance, and side walls. The top wall has an insert plate to flush-mount the test surfaces. The channel flow setup is submerged in the test section of a large free-surface flume. The PIV and micro-PTV cameras image a wall-normal streamwise plane (xy plane) illuminated by a collimated laser sheet with edges parallel to the channel wall to minimize wall reflection.

The velocity averaged along the y direction and the maximum streamwise velocity at the center of the channel are U_b = 0.174 m/s and U_{max} = 0.205 m/s, respectively. The flow rate is kept constant in the flume using an orifice flow meter with an estimated time-averaged variation of ±0.002 m/s in U_b based on repeating the experiments. The Reynolds number based on full channel height (H) is $Re_H = U_bH/\nu$ = 4,400 where ν is kinematic viscosity of water (1.004×10^{-6} m^2/s). The estimated friction velocity is u_τ = 0.0113 m/s while the wall unit (viscous length scale) is $\lambda = \nu/u_\tau$ = 88.8 μm based on the PTV measurements over the smooth acrylic wall as detailed in section II.B. Reynolds number based on frictional velocity is $Re_\tau = u_\tau H/(2\nu)$ = 140. This relatively low Re is chosen to obtain a larger wall unit and improve the relative spatial-resolution of the measurement system in the vicinity of the wall [27]. The DNS of turbulent channel flow at Re_τ = 150 by Tsukahara *et al*. [28] is resented to evaluate the uncertainty of measured turbulent statistics over the smooth wall. The channel dimensions and flow condition are summarized in Table 2. The superscript $^+$ represents parameters normalized using friction velocity u_τ and wall unit λ of the smooth surface. Therefore, the subsequent analysis shows the effect of SHS on turbulence statistics in physical dimensions as common inner scaling is applied. The analysis is also carried out at a constant flow rate, which results in different Re_τ over the two surfaces.

Table 2 The geometric dimensions and flow statistics of the turbulent channel flow. The velocities U_b and U_{max} are measured using PIV while u_τ and λ are obtained using micro-PTV.

Parameter	Dimensions	Value
Channel dimensions ($H\times W\times L$)	mm	25×540×3,000
U_b	m/s	0.174
U_{max}	m/s	0.205
Re_H	-	4,400
u_τ	m/s	0.0113
λ	μm	88.8
Re_τ	-	140

B. Superhydrophobic surface

The SHS is fabricated by spray coating of the acrylic insert plate using a commercial product (Rust-Oleum NeverWet) which deposits a layer of micro- and nano-particles on the surface. This product has been previously applied by Aljallis *et al*. [16], Zhang *et al*. [22], and Vajdi Hokmabad & Ghaemi [23]. The insert module is first cleaned with ethanol and sprayed with a base layer for better adhesion of the superhydrophobic particles. Three layers of the top coat are applied to deposit the mico/nano particles. The surface is allowed to dry for 12 hours. Roughness measurement of a similar surface by Vajdi Hokmabad & Ghaemi [23] using Ambios XP-300 surface profilometer resulted in root-mean-square roughness of R_{rms} = 10.2 μm and peak-to-trough roughness of R_{PT} = 41 μm. Bidkar *et al*. [17] observed DR when the roughness (R_{PT}) of the SHS is an order of magnitude smaller than the thickness of viscous sublayer (~444 μm in the current experiment). The surface roughness normalized by wall unit ($k^+_{rms} = R_{rms}/\lambda$) is 0.11. Further analysis of the life-time of the plastron (i.e., longevity of the SHS) is investigated by scrutiny of the temporal variation of near-wall velocity as detailed in the Appendix section.

C. Particle image velocimetry (PIV)

The turbulent flow across the full-channel is characterized using planar PIV with field-of-view (FOV) of 44.8 × 33.9 mm^2. An Imager Intense CCD camera (LaVision GmbH) with 1376 × 1040 pix sensor (pixel size of 6.45 × 6.45 μm^2, 12-bit resolution) images at magnification of M = 0.2 with digital resolution of 32.6 μm/pix through a f = 105 mm Nikkor lens at aperture size of f / 8. The FOV is located 94H downstream of the channel entrance and 18H downstream of the leading-edge of the insert plate as shown in Fig.1. The laser beam generated by a 400 mJ/pulse Nd:YAG laser (Spectra-Physics) is shaped into a collimated laser sheet with 25 mm width (y direction) and 1 mm thickness (z direction) using a combination of spherical and cylindrical lenses. The edges of the laser sheet are directed parallel to the top wall of the channel (in x direction) to minimize wall reflection. This illumination is carried out using a mirror sealed inside an acrylic column submerged downstream of the channel in the flume, as shown in Fig.1. An ensemble of 8,000 pairs of double-frame images (with laser pulse separation of Δt = 1500 μs) are recorded at 5 Hz. The Δt results in maximum particle displacement of 10 pix in the channel centerline. The camera frames and laser pulses are synchronized using a timing unit controlled by DaVis 7.4 (LaVision GmbH).

The image processing in DaVis 8.3 (LaVision Gmbh) initiates with subtraction of the minimum of the ensemble of the PIV images from each image. The images are also normalized by the average intensity of the ensemble to increase the signal-to-noise ratio before applying the cross-correlation algorithm. Multi-pass cross-correlation with final interrogation window (IW) size of 48×48 pixels (1.5×1.5 mm^2, $17.6^+\times17.6^+$) with 75 percent overlap is applied. The obtained vector fields are post processed by applying the universal outlier detection [29]. The vector range is also limited to 0 to 14 pixels for the U component and -3 to 3 pixels for the V component of the velocity vector. Multi-pass ensemble of correlation (EOC)

with initial interrogation window (IW) size of 96×96 and final IW size of 8×8 pixels (0.2×0.2 mm^2, $2.9^+ \times 2.9^+$) with 75 percent overlap is applied to obtain the mean velocity profile. The location of the top and bottom wall is detected from the intensity peak (I_{max}) of the remaining reflection of the laser sheet at the wall. The I_{max} location is obtained by detecting the local maxima on a plot of intensity versus y averaged over the ensemble of the images and also along x direction. The upper bound uncertainty of this technique is equivalent to the thickness of the glare line, which is estimated using the width of the intensity peak at I_{max}/e^2. This is equivalent to 5 pix (163.5 μm, 1.8^+) as presented in Table 3 along with the parameters of PIV setup. The applied PIV system cannot resolve the smallest turbulent structures (~20^+~1.8 mm) [30] since it is optimized to cover the full channel.

D. Long-range microscopic particle tracking velocimetry (micro-PTV)

Microscopic-PTV with high spatial-resolution is carried out using a second Imager Intense CCD camera (LaVision GmbH) equipped with a Nikkor lens with focal length of f = 200 mm at aperture size of f /11. The lens is connected to 360 mm extension tube (bellows) to allow a working distance of 370 mm. The combination results in magnification of M = 1.6 and digital resolution of 3.92 μm/pix. The estimated depth-of-field of 0.3 mm is smaller than the laser sheet thickness (~1 mm), therefore, presence of out-of-focus particle images is expected. Mirco-PTV measurements are carried out 85H downstream of the channel entrance and 9H downstream of the leading-edge of the insert plate as shown in Fig.1. The FOV is 5.3 mm×4.0 mm in the x and y directions, respectively. An ensemble of 8,000 pairs of double-frame images are recorded with Δt = 1500 μs with maximum displacement of 70 pix in streamwise direction. Minimum intensity subtraction and image normalization is applied before carrying out particle tracking. The number density of the particles in the images is around 4 particles/mm^2. Wall detection has been carried out similar to the method applied to the PIV images. The estimated uncertainty based on the micro-PTV images is 1.5pix = 5.8μm = 0.06^+.

The PTV algorithm was developed in MATLAB to only track the in-focus particles. The algorithm initiates by detection of local maxima larger than a specified intensity threshold. The local maxima are rejected if multiple peaks are detected within a rectangular window of 60×45 pix in x and y directions, respectively. This filter prevents detection of erroneous pairs in the subsequent steps. The area of particle images is estimated and particles outside of 3-10 pixels are rejected. Particle images smaller than 3 pix in area can introduce bias error due to peak locking [31] while particles larger than 10 pix are out-of-focus. The pair detection was carried out using an initial predictor obtained by ensemble of correlations (EOC) of the micro-PTV images [32]. The multi-pass EOC process initiates with window size of 256×256 pixel to detect the large particle movements and follows by smaller window size of 8×8 (31.3×31.3 mm^2) with 75 percent overlap. The PTV algorithm applied the estimated velocity from EOC to search for the particle in the second frame in a (Δx, Δy) = 60×30 pix neighborhood. Only particle pairs with peak intensity ratio of 0.25 – 1.8 are selected for the final sub-pixel peak detection using a Gaussian fit.

The average velocity and high-order turbulence statistics are obtained by averaging the particle velocities sorted in wall-normal bins. The mean velocity profile is obtained by averaging over (Δx, Δy) = 1290×10 pix (5.0×0.04 mm^2, $56.9^+ \times 0.44^+$) bins while the second-order statistics (Reynolds stresses) are obtained by averaging over larger bins with (Δx, Δy) = 1290×100 pix (5.0×0.39 mm^2, $56.9^+ \times 4.4^+$) to ensure statistical convergence.

Table 3 The parameters of the PIV and long-range micro-PTV systems for simultaneous measurement of the outer and inner layer flows, respectively.

	PIV		Micro-PTV		
Magnification	0.2		1.6		
Digital resolution	32.6 μm/pix		3.92 μm/pix		
Time interval Δt	1,500 μs		1,500 μs		
Measurement field	1376×1040 pix 44.8×33.9 mm^2 $504.8^+ \times 381.5^+$		1376×1040 pix 5.3×4.0 mm^2 $60.7^+ \times 45.8^+$		
Accuracy of wall location	± 5 pix ± 163.5 μm $\pm 1.8^+$		± 1.5 pix ± 5.8 μm $\pm 0.06^+$		
Velocity evaluation	Correlation of double-frames	Ensemble of correlations	Particle tracking		Ensemble of correlations
IW/ bin size (Δx, Δy)	48×48 pix 1.5×1.5 mm^2 $17.6^+ \times 17.6^+$	8×8 pix 0.2×0.2 mm^2 $2.9^+ \times 2.9^+$	1209×100 pix 4.7×0.39 mm^2 $53.3^+ \times 4.4^+$	1290×10 pix 5.0×0.04 mm^2 $56.9^+ \times 0.44^+$	24 × 24 pix 0.09×0.09 mm^2 $1.0^+ \times 1.0^+$
IW / bin overlap	75%	75%	75%	75%	75%
Application	Outer layer turbulence	<*U*> across the channel	Inner layer turbulence	<*U*> in the inner layer	Near wall <*U*> (section D)

III. Results

Statistical characterization of the turbulent flow is presented over the superhydrophobic surface (denoted SHS) and the flat acrylic surface (denoted smooth). The SHS and smooth surfaces are placed at the top wall where $y / H = 0$ while the bottom surface is at $y / H = 1$. The bottom surface is always a glass surface in both SHS and smooth experiments.

A. Mean velocity

The semi-logarithmic presentation of normalized mean streamwise velocity ($u^+ = \langle U \rangle / u_\tau$) over the smooth surface obtained from micro-PTV and PIV using EOC method is shown in Fig. 2(a). The PTV profile is in agreement with both the law of the wall ($u^+ = y^+$) in the linear sublayer ($y^+ < 5$) and the logarithmic law ($u^+ = 1/\kappa \ln(y^+) + B$) profile with $\kappa = 0.39$ and $B = 5.5$. The overlap indicates a fully developed turbulent channel flow. There is a small discrepancy between the PIV data and PTV data up to $y^+ \sim 20$ which is associated with bias errors in the near wall PIV measurement. The large PIV interrogation window is the main cause of bias error in the buffer layer where the velocity gradient is large. Closer to the wall and in the viscous sublayer, the mirrored particle images, signal truncation, and the glare of the laser sheet in the near wall interrogation windows are also associated with near-wall error of PIV measurement [33]. The closest data point with no apparent bias error in Reynolds stresses from the PIV measurement is at $y^+ \sim 15$. An investigation of the PIV data using the indicator function, $\zeta^+ = y^+ \, du^+/dy^+$, shows that the log-law is

relatively narrow [34, 35]. The log-law is limited to y^+=50 to 110 based on the flat section of ζ^+ with an assumption of 10% variation.

The profile of <U> over smooth and SHS surface across the channel measured using PIV (EOC method) are shown in Fig. 2 (b). The data is normalized using bulk velocity (U_b) over the corresponding surface. The profile of the smooth surface shows a good symmetry as shown by comparison with the flipped axis profile shown with dashed line in Fig. 2(b). The SHS and smooth profiles overlap across the channel showing no considerable macroscopic difference between the velocity profiles within the spatial-resolution and near-wall limitations of the PIV system. The overlap across the bottom side of the channel over the glass surface ($y / H > 0.5$) shows repeatability of the measurements. Vajdi Hokmabad & Ghaemi [23] also observed overlap of <U> over a smooth and SHS away from the wall at $y^+ > 10$. Their measurement closer to the wall and in particular within $y^+ < 5$ (linear viscus sublayer) was biased due to the strong glare of the laser light from the SHS. PIV measurement of Woolford *et al*. [10] over a superhydrophobic surface manufactured by photolithography (24 μm wide longitudinal cavities) also showed no discernable difference at $0.02 < y/H < 0.2$ while they observed a slightly flatter <U> (smaller velocity) over the SHS in the channel core ($0.4 < y/H < 0.6$).

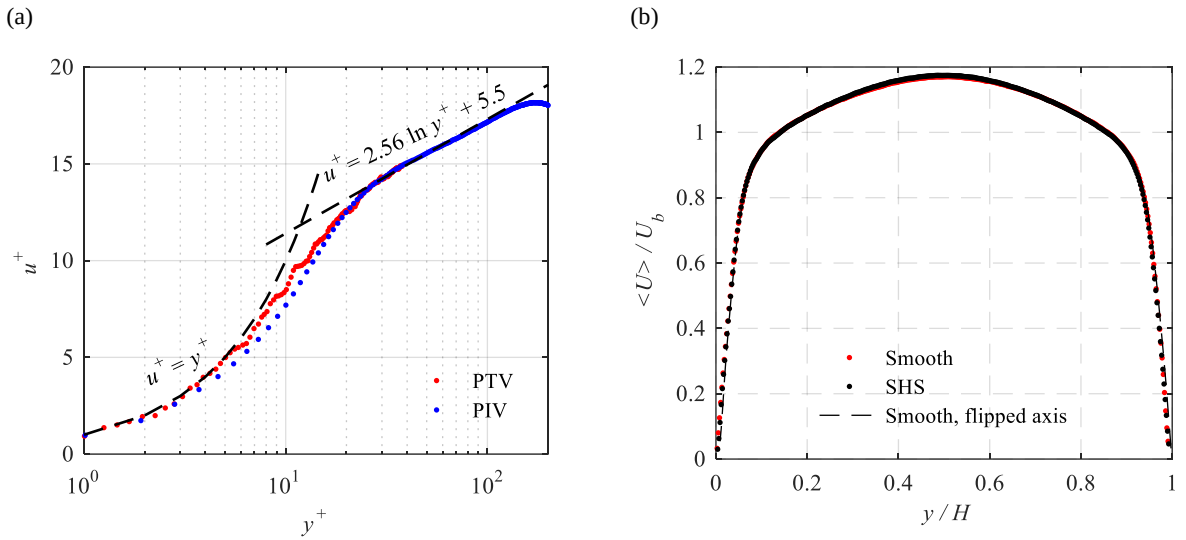

Figure 2 (a) Mean velocity profile over the smooth wall (no-slip wall) obtained from the micro-PTV and PIV (using EOC). (b) Mean streamwise velocity over the smooth and SHS obtained using PIV.

Scrutiny of near-wall velocity is carried out using the long-range micro-PTV measurement. The velocity of individual PTV tracers ($U^+ = U/u_\tau$) over the smooth surface and SHS in the inner layer (y^+<35) are shown in Fig 3 (a) and (b), respectively. The mean velocities obtained from averaging the particle velocities in bins with (Δx, Δy) = $56.9^+ \times 0.44^+$ dimensions are also shown in these figures. The presence of the no-slip boundary condition is evident over the smooth surface as the mean velocity approaches zero at the wall ($y^+ = 0$). The detected tracers also have a negligible velocity in the immediate vicinity of the smooth wall. There is a large number of particles with finite velocity $1 \leq U^+ \leq 4$ (0.011 m/s $\leq U \leq$ 0.044 m/s) at the immediate vicinity of the SHS. The estimated mean slip velocity is U_s = 0.023 m/s (U^+ = 2.1) at y^+= 0 over the SHS which is about 13% of the bulk velocity (U_b). Ling *et al*. [18] reported slip velocities in the order of 14.5 to 36.5% of U_b (0.29 to 0.73 m/s or 3.2^+ to 9.6^+) on different SHSs with k^+_{rms} ranging from 0.43 and 3.28. Ou & Rothstein [36] observed a slip velocity with $0.6U_b$ magnitude over ultra-hydrophobic surface in a laminar microchannel.

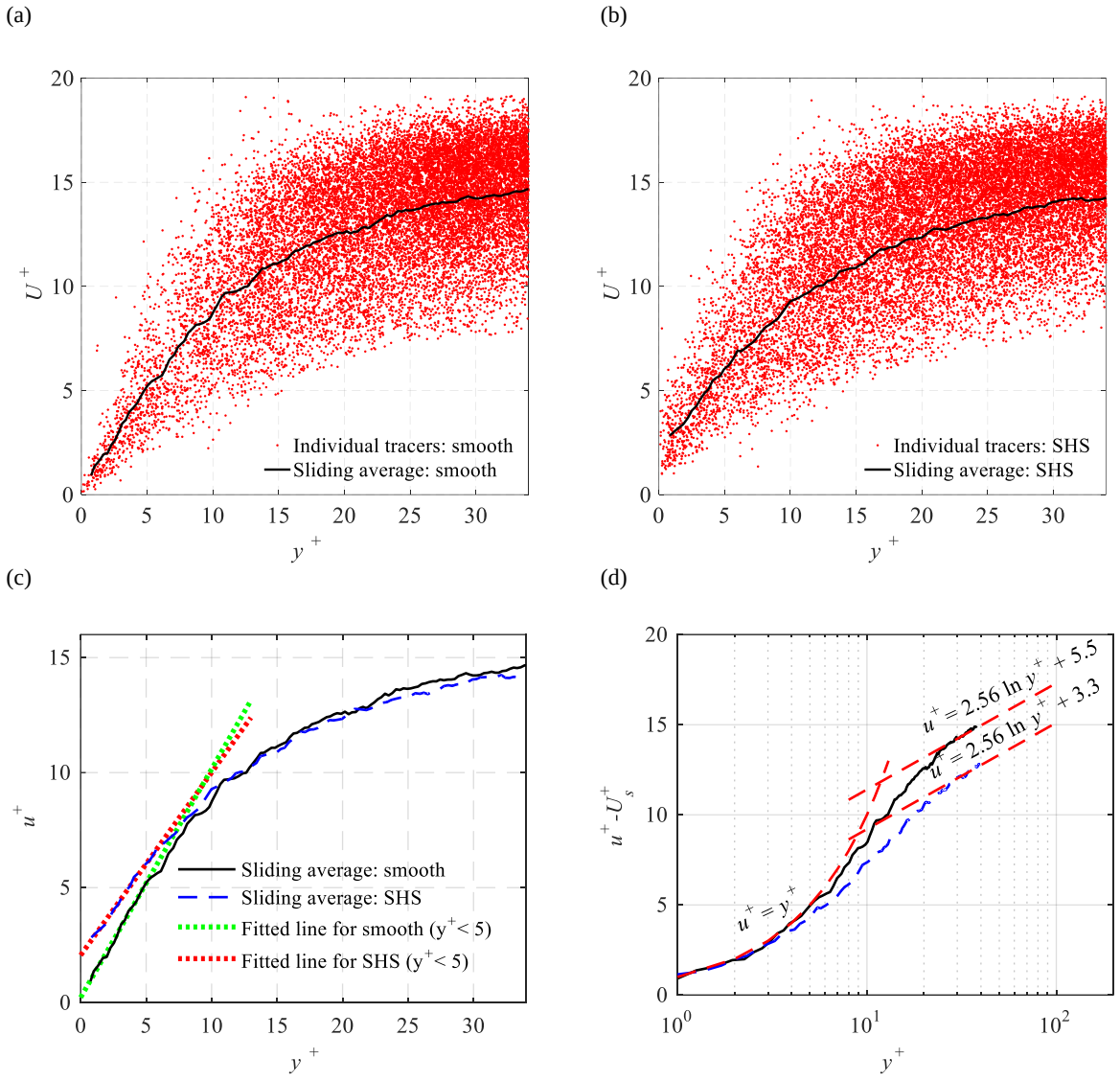

Figure 3 The velocity of tracer particles from micro-PTV over (a) smooth surface and (b) SHS. (c) The mean velocity over the smooth and SHS obtained from averaging the velocity of the tracer particles in bins with wall-normal dimension of 40 μm (0.44^+) and 75% overlap. (d) Semi-logarithmic representation of the mean velocity relative to the estimated slip velocity at the wall (u^+-U_s^+).

The mean profile obtained using sliding average over the velocity of tracers is shown in Fig 3(c) to scrutinize the gradient and the slip length over the smooth and SHS surfaces. The velocity gradient $\partial\langle U\rangle/\partial y$ of the linear viscous sublayer ($y^+ < 5$ with 20 data points) reduces by about 19% over the SHS as shown by the fitted lines in Fig 3(c). As a result, the friction velocity over the SHS reduces to 0.0102 m/s and the corresponding Re_τ= 127. This value is similar to the 18% DR reported by DNS of Rastegari & Akhavan [1] with an assumed slip velocity of $U_s = 0.15U_b$. The $\partial\langle U\rangle/\partial y$ estimation over the SHS results in a slip-length of about l_s = 200 μm (2.2^+). The accuracy of the wall location (available in Table 3) is about 0.06^+ and does not affect the estimated slip length. The u^+ over the smooth surface is smaller than that of the SHS at $y^+ <$ 10 as observed in Fig. 3(c). The theoretical work of Fukagata *et al*. [24] also predicts increase of $\langle U\rangle$ in

the vicinity of the wall as a result of the wall slip while $<U>$ reduces further away from the wall to conserve the mass flow. The DNS of Jung *et al*. [14] also shows evidence of increase of mean velcoity in the near wall region ($y / H < 0.2$) with increase of the air-layer thickness while reduction of mean velcity is observed further away from the wall. The holographic measurements of Ling *et al*. [18] in the inner layer also indicated increase of the near-wall mean velocity.

Fig 3 (d) shows semi-logarithmic plots of mean velocity profiles with subtracted slip velocity (u^+-U_s^+) for the SHS relative to the smooth wall. The u^+-U_s^+ over the SHS overlaps with the smooth surface profile in the linear viscous sublayer ($y^+ < 3$) while a downward shift of u^+-U_s^+ with respect to the smooth wall is observed further away from the wall. The fitted logarithmic line over the SHS has a smaller B of 3.3. Min & Kim [9] also confirm a downward shift in the buffer and log layers of the SHS when combined streamwise and spanwise wall slip is imposed in their DNS. The u^+-U_s^+ versus y^+ of the smooth and the SHS collapsed when only a streamwise slip was applied in their DNS. This indicates presence of combination of streamwise and spanwise slip over the SHS of the current study with random texture. The DNS of Rastegari & Akhavan [1] has also confirmed the downward shift of the log-layer and thinner buffer layer over the SHSs.

B. Reynolds shear stress

The profiles of Reynolds shear stress $<uv>$ across the channel and in the near-wall region of $y^+< 35$ are measured using planar PIV and micro-PTV and plotted in Fig. 4 (a) and (b), respectively. The $<uv>$ profile of the smooth wall in Fig. 4 (a) shows perfect symmetry when compared with the flipped profile shown as red solid line. A linear variation of $<uv>$ over the smooth surface is observed in the mid-section ($0.2<y/H<0.7$) of the channel which confirms the fully developed state of the turbulent channel flow. The $<uv>$ profiles of smooth and SHS overlap across the bottom half of the channel (y / H = 0.5 to 1) as the common glass wall is located at $y / H = 1$ for both cases. The $<uv>$ profile from DNS of Tsukahara *et al*. [28] at $Re_\tau = 150$ is also shown on the lower half of the channel (y / H = 0.5 to 1) for comparison with the measurement over the flat surface. There is a small discrepancy between the measured data and the DNS which is attributed to the lower $Re_\tau = 140$ of the current work.

The intercept of the fitted line over the linear region $<uv>$ profile in the upper-half of the channel (i.e., y / H = 0.2 to 0.5) with the wall $y / H = 0$ can be used to estimate the wall-shear stress (τ_w). The results show 7.2% reduction of the intercept of the fitted line and consequently wall shear stress over the SHS. The uncertainty of this method to obtain the wall-shear stress is estimated according to Hou *et al*. [37] using

$$\tau_w = \rho u_\tau^2 \left(1 \pm \frac{\varepsilon_{uv}}{0.6u_\tau^2}\right)\left(1 \pm \frac{\varepsilon_y}{0.5H}\right) \quad (1)$$

Here ε_{uv} is the error in the measurement of $<uv>$ and is equal $0.03u^2{}_\tau$ with the assumption of 0.1 pix uncertainty in the instantaneous velocity of PIV. The ε_y is the error in estimation of the location of the mid-channel and is assumed to be 0.5 pix~ 0.18λ. Eq.1 can be simplified as

$$\tau_w = \rho u_\tau^2 (1 \pm 0.05) \quad (2)$$

where the uncertainty of τ_w is about 5%. The peak value of $<uv>$ is also reduced by about 7.4% over the SHS while its wall-normal distance stays at $y/H \sim 0.1$ (28^+) and within the spatial-resolution of the PIV system (17.6^+). The underestimation of DR relative to the previous estimation based on $\partial<U>/\partial y$ of micro-PTV is associated with relatively short length of the SHS surface ($22.8H$). Microscopic PTV measurement in Fig. 4 (b) shows that $<uv>$ over the SHS is slightly larger than the smooth surface at $y^+<10$ while it

becomes smaller further away from the wall beyond y^+>10. At y^+ = 35, <*uv*> over the SHS is ~30% smaller than that of the smooth surface. This is qualitatively in agreement with the outer layer PIV measurement of Fig. 4 (a). PIV showed reduction of <*uv*> peak over the SHS although underestimated the reduction due to spatial-resolution limitations.

The PIV of Woolford *et al*. [10] showed overlap of <*uv*> profiles on the half of the channel where the common flat surface was located while <*uv*> over the SHS becomes gradually smaller than that of the smooth surface with approaching the SHS wall. They observed about 8% reduction of <*uv*> peak intensity with no displacement of its location over the investigated SHS with 11% DR. Vajdi Hokmabad & Ghaemi [23] observed 15% reduction of <*uv*> peak intensity over their SHS with roughness of k^+_{rms} = 0.11 with slight shift of the peak location away from the wall (~5λ). The DHM of Ling *et al*. [18] over SHSs with k^+_{rms}= 0.43, 0.62, and 0.89 showed a larger <*uv*> over the SHSs at y^+<15 followed by smaller <*uv*> over the SHS at 15<y^+<100. This trend is consistent with the current investigation although the increase of <*uv*> at y^+<15 over the rough SHSs of Ling *et al*. [18] is larger. Ling *et al*. [18] also observed increase of <*uv*> across their measurement domain (2 < y^+ < 200) over SHSs with larger roughness of k^+_{rms} = 1.71 and 3.28.

The DR percentage is also estimated using the analytical expression provided by Rastegari & Akhavan [1] for surfaces with slip velocity based on initial formulation of Fukagata *et al*. [38]. They suggested DR is the summation of two terms, which includes slip velocity at the wall, and a weighted wall-normal integral of Reynolds shear stress. This equation is expressed as

$$\mathrm{DR} = \frac{U_s}{U_b} + \left(1 - \frac{U_s}{U_b}\right)\left(\frac{3\varepsilon}{1 - 3I^+}\right) \tag{3}$$

where $\varepsilon = I^{+0} - I^+$ is the difference between the integrals of weighted Reynolds shear stress over the smooth surface (I^{+0}) and SHS (I^+), respectively. I^+ is defined as

$$I^+ = \int_0^1 (1-\delta)\langle uv\rangle^+ d\delta \tag{4}$$

Here $\delta = 2y / H$ is the normalized wall-normal coordinate. The integrals are obtained within δ = 0.01 to 0.16 (or from 1.4$^+$ to 22.5$^+$) using micro-PTV and continued from δ = 0.16 to 1.0 (22.5$^+$ to 140$^+$) using PIV. The obtained DR from equation (3) is 21.9% over the current SHS. The corresponding friction velocity and Re_τ are 0.010 m/s and 125, respectively. This value of DR is close to the estimated DR of 19% obtained from the velocity gradient ∂<*U*>/∂y as shown in Fig. 3 (c).

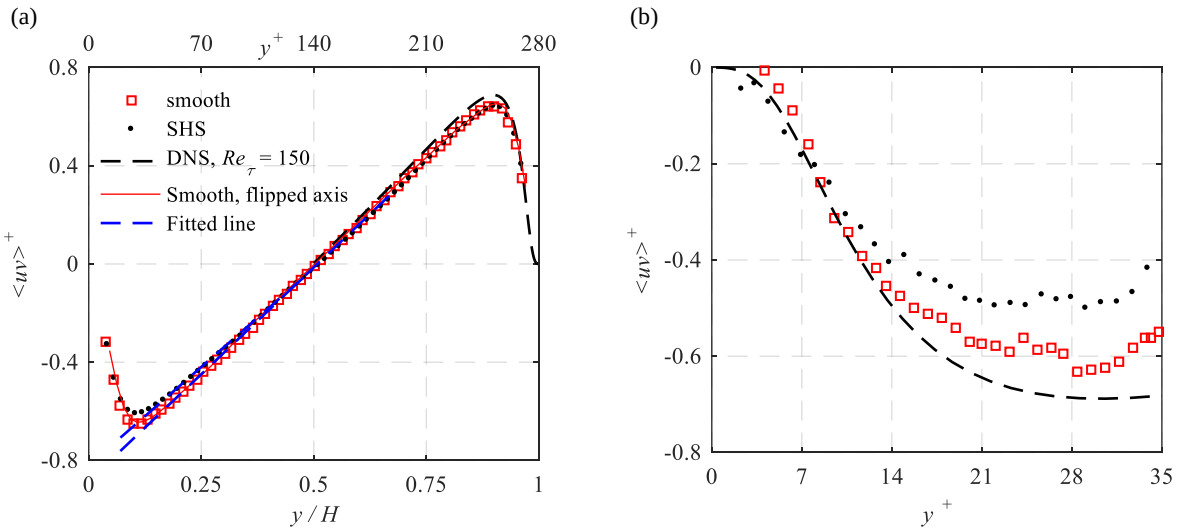

Figure 4 (a) Measurement of Reynolds shear stress using PIV over smooth and SHS across the full channel. The wall-normal distance is normalized using both the channel height (H) and inner scaling (λ) as shown in the lower and upper x-axis, respectively. The SHS surface is placed at $y/H = 0$ while the top wall at $y/H = 1$ is a smooth glass wall for both smooth and SHS cases. The DNS data of Tsukahara *et al*. [28] is provided for comparison over the bottom half of the channel. (b) Inner layer measurements of $<uv>$ using micro-PTV.

C. Normal Stresses

The streamwise component of normal Reynolds stress, $<u^2>/u_\tau^2$, is obtained from the PIV and shown in Fig. 5 (a) to evaluate its distribution across the channel. DNS of Tsukahara *et al*. [28] at $Re_\tau = 150$ is also shown in the lower half of the channel for comparison. The near-wall peak of $<u^2>$ is not captured due to the limited spatial-resolution of the current PIV. The $<u^2>$ profile of the smooth surface overlaps with the $<u^2>$ profile plotted with flipped y/H axis. This shows the symmetry of the channel flow. No considerable difference is observed between $<u^2>$ profile of the smooth and SHS away from the walls at $y/H > 0.1$. The PIV of Vajdi Hokmabad & Ghaemi [23] with slightly better spatial-resolution (14.6λ) showed smaller $<u^2>$ over the SHS with respect to the smooth surface till about $y^+ \sim 100$ followed by overlap of the profiles further away from the wall. The outer layer measurement of Woolford *et al*. [10] also showed 20% reduction in $<u^2>$ over the SHS at $y / H = 0.2$, which extends till $y / H = 0.8$ into the other half of the channel. The thickness and morphology of the plastron and the length of the SHS may have contributed to the observed differences of these outer layer measurements.

The inner layer measurement of $<u^2>$ within $y^+<35$ from micro-PTV over the SHS and the smooth surface is shown in Fig. 5(b). In the immediate vicinity of the wall at $y^+ < 7$, $<u^2>$ is lightly larger over the SHS relative to the smooth surface. The magnitude of $<u^2>$ peak over the SHS and the smooth surface is similar. However, the location of the peak is closer to the wall over the SHS ($y^+ \sim 9.8$) compared to the smooth surface ($y^+ \sim 15.2$). Further away from the wall at $y^+ > 20$, $<u^2>$ over the SHS becomes comparable with the smooth wall. The DNS of Busse & Sandham [11] also reported larger values of $<u^2>$ over SHS at about $y^+<10$ and an overlap with the smooth case at $y^+>10$ for an imposed streamwise slip length $l^+_s > 0.6$. The DNS of Min & Kim [9] demonstrated that $<u^2>$ over a SHS with both streamwise and spanwise slip is larger at $y^+ < 8$ while it becomes smaller at $8 < y^+ < 100$. DNS of Rastegari & Akhavan [1] over SHSs with longitudinal micro-grooves also observed larger $<u^2>$ at $y^+< 7$ relative to the smooth surface. They associated it with the thinner buffer layer and the downward shift of the logarithmic layer over SHSs. They observed an approximate overlap of $<u^2>/u_\tau^2$ of SHS and smooth surfaces away from the wall if $<u^2>$ is normalized with the u_τ of the corresponding surface. However, dimensional $<u^2>$ over the SHS is smaller

in the outer layer. The holographic measurement of Ling *et al*. [18] showed for SHSs with $0.43 \leq k^{+}_{rms} \leq 1.71$, the value of $\langle u^2 \rangle$ is larger than the smooth case at $y^{+}<10$ with the peak closer to the wall. At $10 \leq y^{+} \leq 100$, $\langle u^2 \rangle$ is smaller than the smooth surface for these SHSs. They also reported smaller magnitude of $\langle u^2 \rangle$ peak at larger DR. In general, simulations and experiments show SHSs increase $\langle u^2 \rangle$ in the inner layer (linear sublayer and buffer layer) while reduce $\langle u^2 \rangle$ in the outer layer.

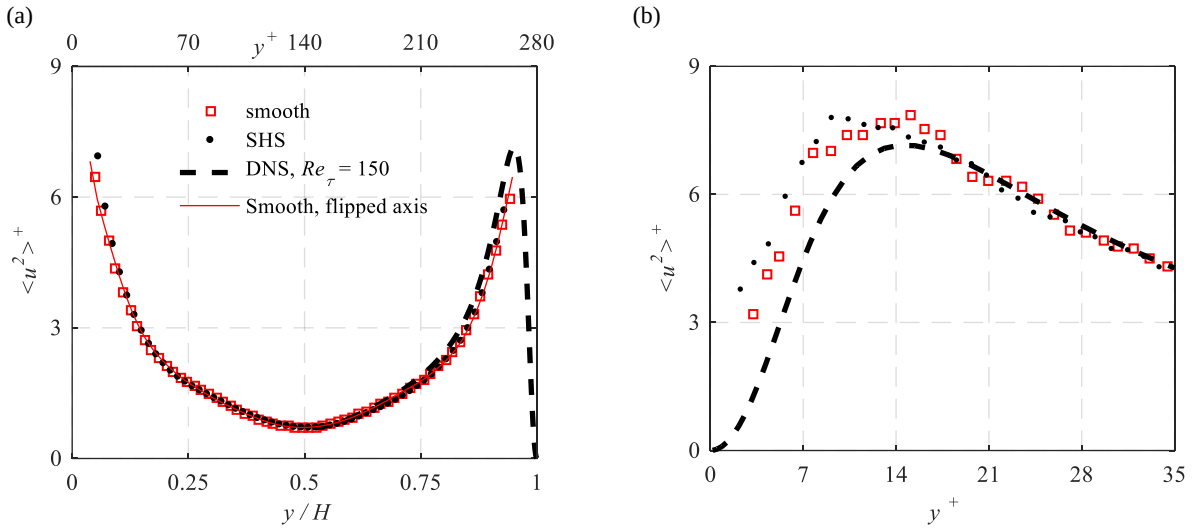

Figure 5 (a) Measurement of $\langle u^2 \rangle$ using PIV over smooth and SHS. The wall-normal distance normalized using the outer (H) and inner scaling (λ) are shown in the lower and upper x-axis, respectively. DNS of Tsukahara *et al*. [28] is provided for comparison over the bottom half of the channel. (b) Measurements of $\langle u^2 \rangle$ within the inner layer using micro-PTV.

The wall-normal component of Reynolds stress, $\langle v^2 \rangle$, is shown in Fig. 6 (a) from PIV measurement over both surfaces across the channel. The $\langle v^2 \rangle$ profiles of the smooth and SHS overlap across most of bottom-half of the channel although there are discrepancies near the bottom wall at $y/H > 0.85$. However, $\langle v^2 \rangle$ peak values of the two surfaces at $y/H \sim 0.8$ overlap. The smaller peak value relative to the DNS of Tsukahara *et al*. [28] is attributed to the smaller Re_τ of the current experiment and also the spatial averaging of PIV. The symmetry of the $\langle v^2 \rangle$ profile of the smooth is also evident from comparison with the flipped data as shown by the red line. The peak of $\langle v^2 \rangle$ over SHS at $y / H = 0.18$ (or $y^{+} = 51$) is reduced by about 5% relative to the peak value over the smooth surface. The location of $\langle v^2 \rangle$ peak is also fixed within the spatial-resolution of the PIV system (17.6^{+}). The difference of $\langle v^2 \rangle$ profiles decreases with reduction of wall-normal distance as they overlap at $y/h = 0.05$ ($y^{+} = 15$).

The normalized $\langle v^2 \rangle$ in the inner layer of $y^{+} < 35$ is shown in Fig. 6 (b) from micro-PTV measurements. The $\langle v^2 \rangle$ over SHS and smooth surface are observed to overlap near the wall at $y^{+}<10$. Beyond $y^{+}>10$, $\langle v^2 \rangle$ over the SHS becomes smaller than the smooth surface. About 30% reduction of $\langle v^2 \rangle$ is observed at $y^{+}=30$. The experiments of Vajdi Hokmabad & Ghaemi [23] showed 13% reduction in $\langle v^2 \rangle$ peak over SHS while the peak moved away from the wall by ~15 wall unit. Woolford *et al*. [10] also observed about 5% reduction of $\langle v^2 \rangle$ extended to core of the channel flow. Min & Kim [9] observed an overlap of $\langle v^2 \rangle$ over the SHS and smooth surface at $y^{+}<8$ but smaller $\langle v^2 \rangle$ over the SHS further away from the wall at $y^{+}>8$. The DNS of Rastegari & Akhavan [1] shows slightly smaller $\langle v^2 \rangle$ in the near wall when the applied slip velocity is 15% of U_b (similar to the present work). In general, the DNS of Min & Kim [9], Rastegari & Akhavan [1] and the current micro-PTV measurement show negligible change of $\langle v^2 \rangle$ in the viscous sublayer. However, Ling *et al*. [18] observed an increase of $\langle v^2 \rangle$ over the SHSs in the inner layer with $y^{+}<$ 10-30 depending on the roughness of the surface. This difference is associated with larger roughness of surfaces tested by Ling

et al. [18] compared to the current experiment and DNS with assumption of a flat surface. Further away from the wall, all experiments (e.g., Woolford *et al*. [10] and Hokmabad & Ghaemi [23]) and simulations (e.g., Min & Kim [9], Rastegari & Akhavan [1]) with DR show reduction of $\langle v^2 \rangle$ relative to that of the smooth wall.

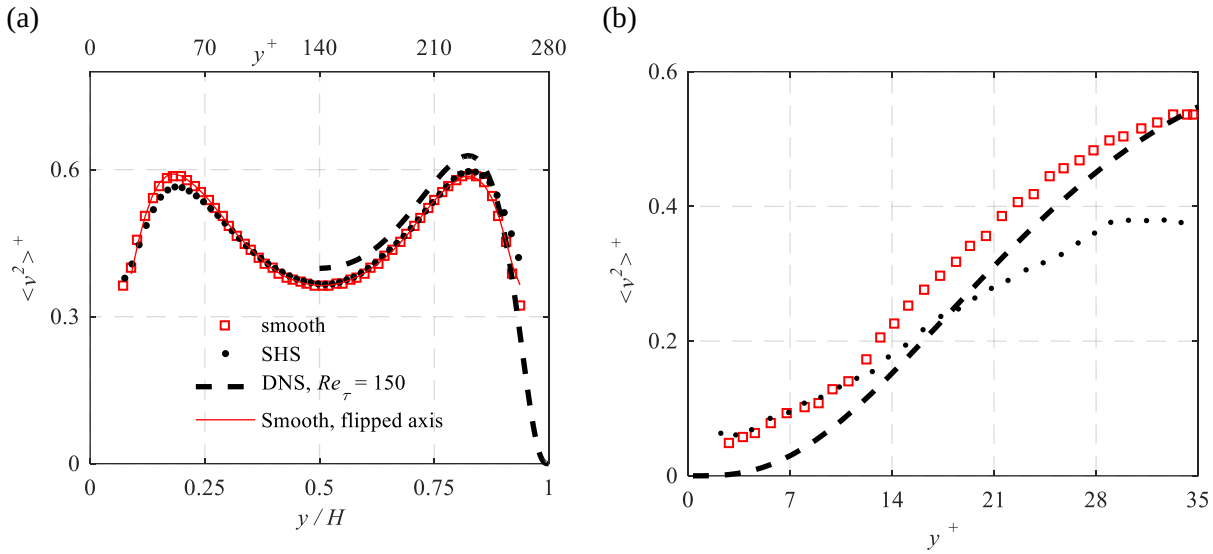

Figure 6 (a) Measurement of $\langle v^2 \rangle$ using PIV over smooth and SHS. The wall-normal distance normalized using the outer (H) and inner scaling (λ) as shown in the lower and upper x-axis, respectively. The SHS surface is placed at $y/H = 0$ while the top wall at $y/H = 1$ is a smooth glass wall for both smooth and SHS cases. The DNS data of Tsukahara *et al*. [28] is provided for comparison over the bottom half of the channel. (b) Inner layer measurements of wall-normal shear stress using micro-PTV.

The joint probability density function (JPDF) of u and v velocity fluctuations from micro-PTV is plotted in Fig. 7 (a) to investigate the correlation of the fluctuations over the SHS. The data is associated with $y^+ = 20$-30 range for statistical convergence of the JPDF. The separate PDFs of u and v are also shown in Fig. 7(b) and (c). The area enclosed by the contours in the sweep quadrant (i.e., $u > 0$ and $v < 0$) for the SHS is similar to the smooth surface. However, the enclosed area by the contours in the ejection quadrant ($u < 0$ and $v > 0$) is smaller over the SHS relative to the smooth surface. The principle axis of the fluctuations has also tilted towards u axis over the SHS, indicating ejection motions with smaller angle with respect to the wall (smaller v). This modification to turbulent fluctuations is also observed in the PDF plots. A negligible change of u distribution is observed in Fig. 7(b), while the PDF of v over the SHS in Fig. 7(c) becomes narrower with a larger peak at $-0.5 < v/u_\tau < 0.5$. The latter shows that there is a larger number of weak v fluctuations and smaller number of strong v fluctuations over the SHS surface. Therefore, the slip boundary condition has resulted in attenuation of ejection motions in $y^+ = 20$-30 range.

(a)

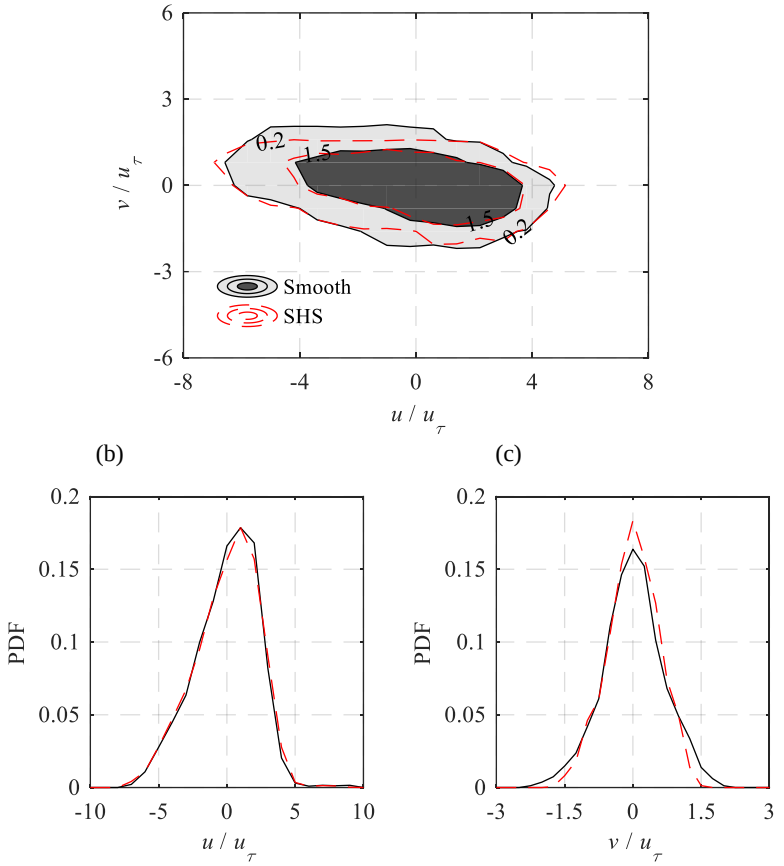

Figure 7 (a) The JPDF of u and v fluctuations in the buffer layer y^+=20-30. The filled contours represent the JPDF over the smooth surface and the lines contours in red show the JPDF over the SHS. The dark gray and the light gray colors represent the 1.5%, and 0.2% JPDF values, respectively. The 2D PDF of (b) the u and (c) v fluctuations. The solid lines (——) in PDF represent the smooth surface while the dashed red lines (-- --) show the PDF of the SHS.

The JPDF of u and v velocity fluctuations in the wall-normal range of y^+ = 5-15 over the SHS and smooth surface is shown in Fig. 8 (a). The effect of slip velocity at this range is different relative to the y^+=20-30 range. The sweep events in the fourth quadrant ($u > 0$, $v < 0$) are attenuated while the ejection motions ($u < 0$, $v > 0$) appear to have a similar JPDF as the smooth surface. This attenuation of sweep events is associated with reduction of the intensity of strong u fluctuations as observed in in the PDF of Fig. 8 (b) at about $u/u_\tau = \pm 6$. The PDF of v fluctuation in Fig. 8 (c) does not show a significant variation of v fluctuations over the SHS in comparison with the smooth surface.

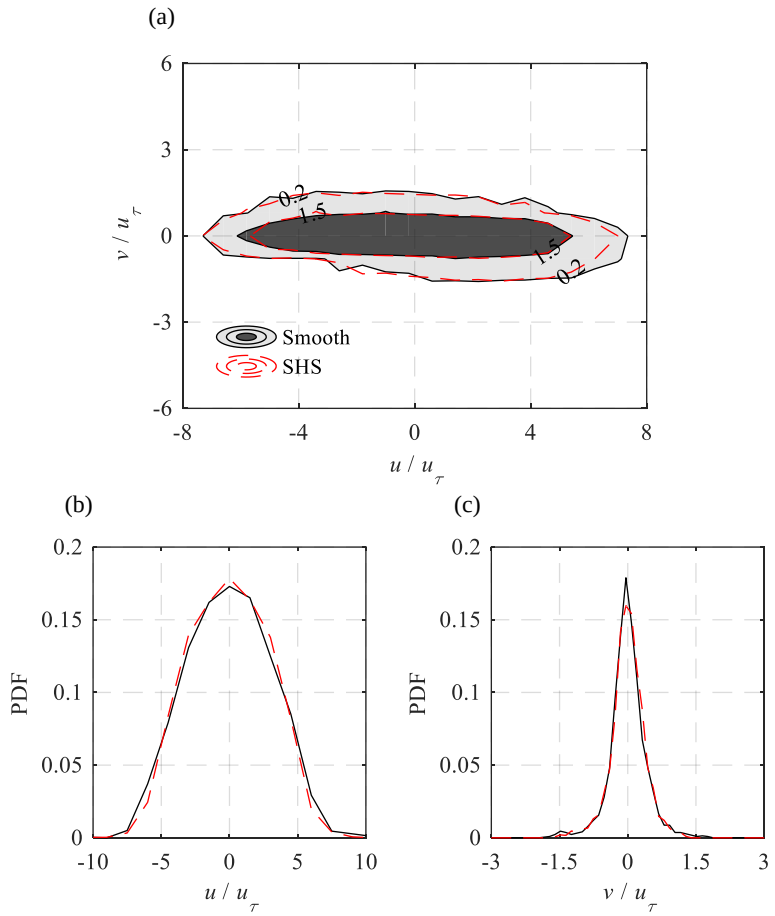

Figure 8 (a) The JPDF of u and v fluctuations in the buffer layer y^+=5-15. The filled contours represent the JPDF over the smooth surface and the lines contours in red show the JPDF over the SHS. The dark gray and the light gray colors represent the 1.5%, and 0.2% JPDF values, respectively. The 2D PDF of (b) the u and (c) v fluctuations. The solid lines (----) in PDF represent the smooth surface while the dashed red lines (-- --) show the PDF of the SHS.

IV. Discussion

The investigation showed that the applied SHS with random texture reduces drag by ~20% due to the 200 μm slip length. The comparison of Reynolds stresses over the SHS and smooth surface is carried out at a constant flow rate while the Reynolds stresses are normalized using a common inner scaling. The results showed that $\langle uv \rangle$ and $\langle u^2 \rangle$ increase over the SHS at the near-wall region of $y^+ < 10$. However, $\langle v^2 \rangle$ over the SHS stays comparable to the smooth surface within $y^+ < 10$. Ling *et al*. [18] observed increase of all three $\langle uv \rangle$ and $\langle u^2 \rangle$, and also $\langle v^2 \rangle$ over the SHS within $y^+ < 10$ while the flow rate was kept constant. The percentages of increase in Reynolds stresses based on the experiment of Ling *et al*. [18] is also larger than those of the current study as it is detailed in Table 1. The larger increase is associated with larger roughness (larger k^+_{rms}) as presented Fig. 9. In this figure, the variation of Reynolds shear stress is defined as $\Delta\langle uv \rangle = ([\langle uv \rangle_{SHS} - \langle uv \rangle_{smooth}]/\langle uv \rangle_{smooth})$, and estimated from Ling *et al*. [18] and the current investigation at $y^+ = 10$. The results, presented versus the surfaces roughness (k^+_{rms}), show a linear increase of $\langle uv \rangle$ with increase of roughness. However, the larger Reynolds shear stress in the near wall region of the SHSs does not necessarily indicate drag increase as the total drag also depends on the slip velocity. The dependence of total drag on Reynolds shear stress and slip velocity is observed in Equation 3. It is important to note that the current investigation has been carried out a low Re_τ and the results cannot be extended to surfaces

with lower roughness at the higher Re_τ of Ling et al. [18]. However, the current investigation is suitable for evaluation of DNS at low Re_τ such as Min & Kim [9] and Rastegari & Akhavan [1].

The experiments of the current study and also Ling *et al*. [18] are both carried out at a constant flow rate. Therefore, the friction velocity and Re_τ reduce in case of drag reduction. If Reynolds stresses are scaled based on the corresponding friction velocity (i.e., $u_{\tau s}$ = 0.0100 m/s of the SHS instead of u_τ = 0.0113 of the smooth surface) where $u_{\tau s}$ is the friction velocity of the SHS, the non-dimensional Reynolds stresses of the current work show a large increase of $\langle u^2\rangle/u^2_\tau$ over the SHS with respect to the smooth at $y^+ < 20$ as illustrated in Fig. 10. Farther away from the wall at $y^+ > 20$, the scaling of all Reynolds stresses based on the corresponding friction velocity results in the overlap of the smooth and SHS profiles.

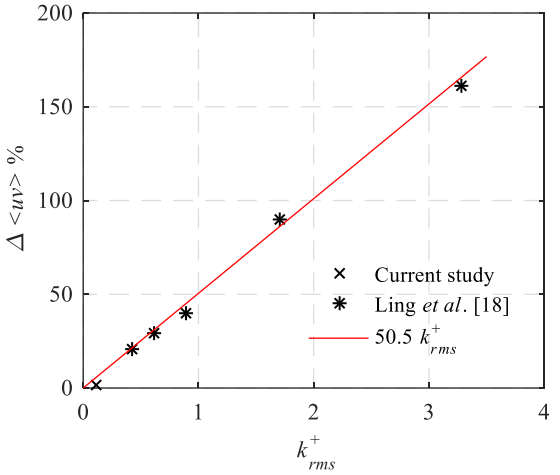

Figure 9 Variation of Reynolds shear stress over SHS in comparison with the smooth surface at y^+ = 5 versus the surface roughness (k^+_{rms}).

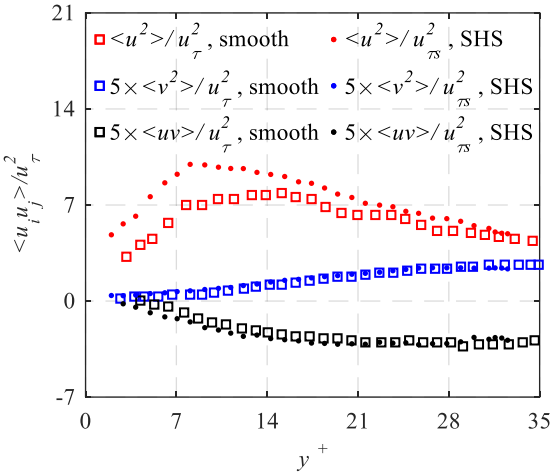

Figure 10 Inner layer measurement of Reynolds stresses using micro-PTV over smooth and SHS. The Reynolds stresses are normalized by the corresponding friction velocity of each surface. The $\langle uv\rangle$ and $\langle v^2\rangle$ are multiplied by a factor of 5 for clarity.

V. CONCLUSION

The magnitude of slip velocity and the effect of SHS on Reynolds stress in the inner and outer layers have been experimentally investigated using simultaneous long-range micro-PTV and macroscopic PIV. The micro-PTV results show a slip velocity of 0.023 m/s over the SHS (13% of U_b) at Re_τ = 140 which corresponds to 200 μm slip-length. The drag is reduced by 19% based on $d\langle U\rangle/dy$ in the linear viscous sublayer and 22% based on the analytical expression of Rastegari & Akhavan [1].

The analysis on turbulence statistics reflects the variations in physical dimensions if the measured Reynolds stresses are normalized using a common inner scaling. The results at a constant flow rate demonstrate a slight increase of $\langle u^2\rangle$ while $\langle v^2\rangle$ stays constant at $y^+<10$ over the SHS relative to the smooth surface. The increase of $\langle u^2\rangle$ is associated with the slip velocity at the wall and has resulted in a small increase of Reynolds shear stress at the wall. Although $\langle u^2\rangle$ slightly increases the PDF of u fluctuations shows attenuation of the strong sweep motion ($\pm u_\tau$) over the SHS. The small increase of Reynolds shear stress at $y^+<10$ has a negligible effect on to the total reduction of wall shears (~20%). The effect of slip-velocity on turbulence production is more pronounced further away at $y^+>15$. In this region, up to 30% reduction of both $\langle v^2\rangle$ and consequently $\langle uv\rangle$ is observed. The scrutiny of the v versus u quadrants shows that reduction of $\langle v^2\rangle$ is associated with attenuation of ejection motions while the sweeps are not affected. The peak of $\langle u^2\rangle$ over the SHS has also moved to y^+=10 relative to the peak location over the smooth

surface which is at y^+=15. The latter indicates a thinner viscous sublayer over the SHS which is in agreement with observed shift of the logarithmic layer toward the wall. If Reynolds stresses are scaled based on the corresponding friction velocity, the non-dimensional stresses show a large increase of $<u^2>/u^2_\tau$ and a small increase of $<uv>/u^2_\tau$ over the SHS with respect to the smooth at $y^+ < 20$. Farther away from the wall at $y^+ > 20$, the scaling of all Reynolds stresses based on the corresponding friction velocity results in overlap of all the Reynolds stress pairs of the smooth and SHS.

The measured turbulence statistics in the inner layer are in agreement with previous DNS of SHS. Therefore, the assumption of planar boundary condition is applicable to the current SHS with relative roughness of k^+_{rms}=0.11 at low Re_τ. The investigation of this SHS with relatively small roughness also indicates the possibility of reducing the adverse effects of roughness on the wall-shear stress.

ACKNOWLEDGEMENTS

This work has been supported by the Natural Sciences and Engineering Research Council of Canada (NSERC RGPIN 1512 GHAEMI and STPGP 478987 SHANKAR).

APPENDIX: ANALYSIS OF SURFACE STABILITY

Drag reduction over a SHS depends on the topology and lifetime of the air layer (plastron). Several repeats of PIV and micro-PTV experiments showed occasional failure of the surfaces (~30% of the tests) and lack of DR, which is speculated to be due to partial or total loss of the air-layer over the SHS. The presence of PIV/PTV tracers, small variations of pH and oxygen level in the flume (~2000 liters of tap water) may have contributed to the inconsistencies. The pH and oxygen level of the water was monitored to be between 7.9-8.1 and 8.3-8.4 mg/L in all the experiments. The manufacturing repeatability and surface defects can also affect the DR.

Two data sets are introduced here as "stable" and "unstable" plastrons to characterize the longevity of the SHS surfaces. The stable data belongs to the SHS experiment detailed in section III. The unstable data is associated with a SHS that gradually lost its DR performance. The longevity of the SHS is monitored by applying the EOC method on the first 100 seconds (500 double-frame images) and the last 100 seconds (t= 1,500 – 1,600 sec) of the long-range micro-PTV images. The 100 second interval is chosen as a compromise between statistical convergence and temporal resolution. The convergence and repeatability of this method is evaluated on the smooth surface in Fig. 11 (a). The mean velocity profiles of the initial (t = 0 – 100 sec) and the final (t =1,500 – 1,600 sec) subsets overlap at y^+<5, showing the statistical convergence of the analysis. The mean velocity at y^+= 0 is also negligible in both subsets indicating the no-slip boundary condition over smooth surface. The results for the initial and final subsets of the stable SHS are shown in Fig. 11 (b). The results confirm the stability of the slip velocity (U_s^+ ~1.5-2) over time. The detected U_s^+ using the EOC method is smaller than the estimated value using micro-PTV in Fig 3(c) due to the larger spatial-resolution of the EOC. The slip velocity over the unstable SHS in Fig. 11 (c) during t = 0 – 100 sec is slightly smaller than the stable surface. However, in the final subset (t =1,500 – 1,600 sec) of Fig 3(c), U_s^+ approaches zero and the unstable SHS loses its DR performance.

The temporal variation of SHS performance is characterized by averaging the streamwise velocity in the wall-normal range of y^+<15 and also over time intervals of 100 s (moving average). The combined average enhances statistical convergence of the data and is indicated by $<U_t^+>$. The result is shown in Fig. 12 as $u_t^+ = <U_t^+>/u_\tau$ for smooth surface, stable SHS, and unstable SHS. The average velocity over the smooth surface and stable SHS are relatively constant in time while u_t^+ of unstable SHS decreases with time

over t = 0 till 800 s. The velocity over both SHSs started at larger values (u_t^+ = 6.5, ~0.08 m/s) than the smooth surface (u_t^+ = 5.3, ~0.06 m/s). However, after 300 sec the unstable SHS loses the plastron as the mean velocity reduces from u_t^+ of the stable SHS to that of the smooth surface. This investigation highlights the importance of plastron evaluation in large-scale experiments. It also shows the need for simultaneous PIV and micro-PTV of the current investigation to ensure inner and outer layer characterization is carried out over the same plastron.

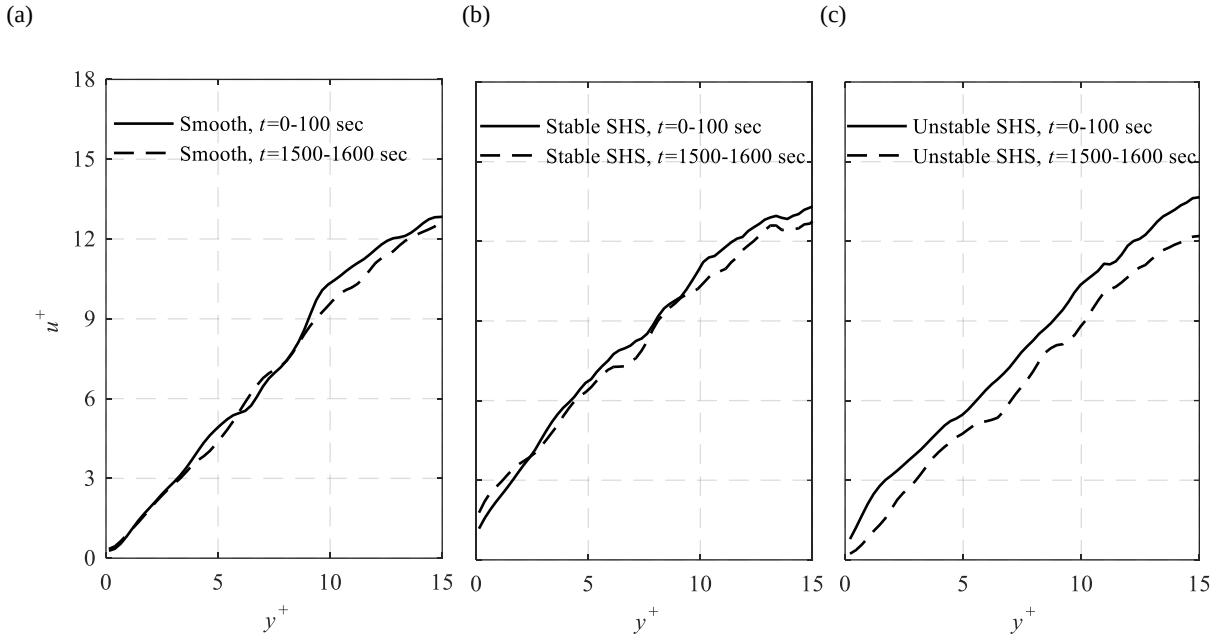

Figure 11 Normalized mean streamwise velocity (u^+) over smooth surface, stable SHS, and unstable SHS obtained from two subsets of the data. The first subset includes the 500 double-frame PTV images from t = 0-100 s and the second subset covers t = 1,500-1,600 s.

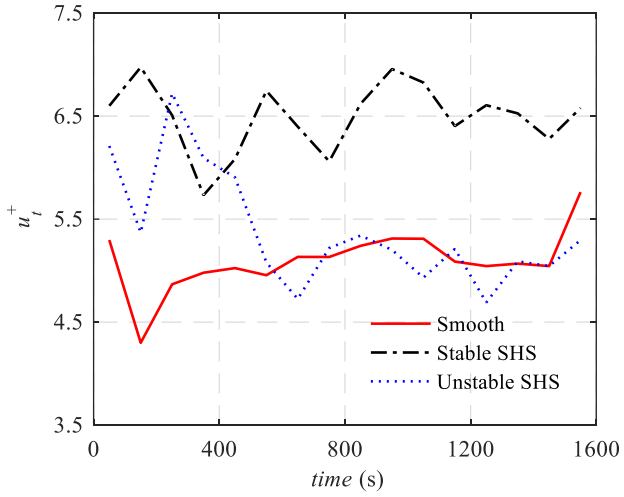

Figure 12 Velocity obtained from micro-PTV is averaged within wall-normal range of y^+=1-15 and with temporal kernel of 100 seconds (500 images pairs) for smooth, stable SHS, and unstable SHS.

REFERENCES

[1] A. Rastegari and R. Akhavan, "On the mechanism of turbulent drag reduction with super-hydrophobic surfaces," *J. Fluid Mech.*, **773**, R4, (2015).

[2] P. Papadopoulos, L. Mammen, X. Deng, D. Vollmer, and H. Butt, "How superhydrophobicity breaks down," *Proc. Natl. Acad. Sci.*, **110**, 3254–3258, (2013).

[3] J. P. Rothstein, "Slip on Superhydrophobic Surfaces," *Annu. Rev. Fluid Mech.*, **42**, 89–109, (2010).

[4] H. Park, G. Sun, and C. J. Kim, "Superhydrophobic turbulent drag reduction as a function of surface grating parameters," *J. Fluid Mech.*, **747**, 722–734, (2014).

[5] M. A. Samaha, H. V. Tafreshi, and M. Gad-el-Hak, "Influence of Flow on Longevity of Superhydrophobic Coatings," *Langmuir*, **28**, 9759–9766, (2012).

[6] B. Vajdi Hokmabad and S. Ghaemi, "Effect of Flow and Particle-Plastron Collision on the Longevity of Superhydrophobicity," *Sci. Rep.*, **7**, 41448, (2017).

[7] J. Ou, B. Perot, and J. P. Rothstein, "Laminar drag reduction in microchannels using ultrahydrophobic surfaces," *Phys. Fluids*, **16**, 4635, (2004).

[8] C.-H. Choi, U. Ulmanella, J. Kim, C.-M. Ho, and C.-J. Kim, "Effective slip and friction reduction in nanograted superhydrophobic microchannels," *Phys. Fluids*, **18**, 87105, (2006).

[9] T. Min and J. Kim, "Effects of hydrophobic surface on skin-friction drag," *Phys. Fluids*, **16**, 0–3, (2004).

[10] B. Woolford, J. Prince, D. Maynes, and B. W. Webb, "Particle image velocimetry characterization of turbulent channel flow with rib patterned superhydrophobic walls," *Phys. Fluids*, **21**, (2009).

[11] A. Busse and N. D. Sandham, "Influence of an anisotropic slip-length boundary condition on turbulent channel flow," *Phys. Fluids*, **24**, 55111, (2012).

[12] M. B. Martell, J. B. Perot, and J. P. Rothstein, "Direct numerical simulations of turbulent flows over superhydrophobic surfaces," *J. Fluid Mech.*, **620**, 31–41, (2009).

[13] R. J. Daniello, N. E. Waterhouse, and J. P. Rothstein, "Drag reduction in turbulent flows over superhydrophobic surfaces," *Phys. Fluids*, **21**, 85103, (2009).

[14] T. Jung, H. Choi, and C. J. Kim, "Effects of the air layer of an idealized superhydrophobic surface on the slip length and skin-friction drag," *J. Fluid Mech.*, **790**, R1, (2016).

[15] K. Watanabe, Y. Udagawa, and H. Udagawa, "Drag reduction of Newtonian fluid in a circular pipe with a highly water-repellent wall," *J. Fluid Mech.*, **381**, S0022112098003747, (1999).

[16] E. Aljallis, M. A. Sarshar, R. Datla, V. Sikka, A. Jones, and C.-H. Choi, "Experimental study of skin friction drag reduction on superhydrophobic flat plates in high Reynolds number boundary layer flow," *Phys. Fluids*, **25**, 25103, (2013).

[17] R. A. Bidkar, L. Leblanc, A. J. Kulkarni, V. Bahadur, S. L. Ceccio, and M. Perlin, "Skin-friction drag reduction in the turbulent regime using random-textured hydrophobic surfaces," *Phys. Fluids*, **26**, 85108, (2014).

[18] H. Ling, S. Srinivasan, K. Golovin, G. H. McKinley, A. Tuteja, and J. Katz, "High-resolution velocity measurement in the inner part of turbulent boundary layers over super-hydrophobic surfaces," *J. Fluid Mech.*, **801**, 670–703, (2016).

[19] A. B. D. Cassie and S. Baxter, "Wettability of porous surfaces," *Trans. Faraday Soc.*, **40**, 546, (1944).

[20] R. Wenzel, "Resistance of solid surfaces to wetting by water," *Ind. Eng. Chem*, **28**, 988–994, (1936).

[21] L. Lei, H. Li, J. Shi, and Y. Chen, "Diffraction Patterns of a Water-Submerged Superhydrophobic Grating under Pressure," *Langmuir*, **26**, 3666–3669, (2010).

[22] J. Zhang, H. Tian, Z. Yao, P. Hao, and N. Jiang, "Mechanisms of drag reduction of superhydrophobic surfaces in a turbulent boundary layer flow," *Exp. Fluids*, **56**, 179, (2015).

[23] B. Vajdi Hokmabad and S. Ghaemi, "Turbulent flow over wetted and non-wetted superhydrophobic counterparts with random structure," *Phys. Fluids*, **28**, 15112, (2016).

[24] K. Fukagata, N. Kasagi, and P. Koumoutsakos, "Erratum: 'A theoretical prediction of friction drag reduction in turbulent flow by superhydrophobic surfaces,'" *Phys. Fluids*, **18**, 89901, (2006).

[25] T. O. Jelly, S. Y. Jung, and T. A. Zaki, "Turbulence and skin friction modification in channel flow with streamwise-aligned superhydrophobic surface texture," *Phys. Fluids*, **26**, 95102, (2014).

[26] S. Türk, G. Daschiel, A. Stroh, Y. Hasegawa, and B. Frohnapfel, "Turbulent flow over superhydrophobic surfaces with streamwise grooves," *J. Fluid Mech.*, **747**, 186–217, (2014).

[27] J. Kim, P. Moin, and R. Moser, "Turbulence statistics in fully developed channel flow at low Reynolds number," *J. Fluid Mech.*, **177**, 133–166, (1987).

[28] T. Tsukahara, Y. Seki, H. Kawamura, and D. Tochio, "DNS of turbulent channel flow at very low Reynolds numbers," in *International symposium on turbulence and shear flow phenomena (TSFP-4)*, 935–940, (2005).

[29] J. Westerweel and F. Scarano, "Universal outlier detection for PIV data," *Exp. Fluids*, **39**, 1096–1100, (2005).

[30] M. Stanislas, L. Perret, and J. Foucaut, "Vortical structures in the turbulent boundary layer: a possible route to a universal representation," *J. Fluid Mech.*, **602**, 327–382, (2008).

[31] C. J. Kähler, S. Scharnowski, and C. Cierpka, "On the uncertainty of digital PIV and PTV near walls," *Exp. Fluids*, **52**, 1641–1656, (2012).

[32] C. D. Meinhart, S. T. Wereley, and J. G. Santiago, "A PIV Algorithm for Estimating Time-Averaged Velocity Fields," *J. Fluids Eng.*, **122**, 285, (2000).

[33] R. Theunissen, F. Scarano, and M. L. Riethmuller, "On improvement of PIV image interrogation near stationary interfaces," *Exp. Fluids*, **45**, 557–572, (2008).

[34] C. M. White, Y. Dubief, and J. Klewicki. "Re-examining the logarithmic dependence of the mean velocity distribution in polymer drag reduced wall-bounded flow." *Phys. Fluids*, **24**, 021701 (2012).

[35] B. R. Elbing, M. Perlin, D. R. Dowling, and S. L. Ceccio. “Modification of the mean near-wall velocity profile of a high-Reynolds number turbulent boundary layer with the injection of drag-reducing polymer solutions.” *Phys. Fluids*, **25**, 085103 (2013).

[36] J. Ou and J. P. Rothstein, “Direct velocity measurements of the flow past drag-reducing ultrahydrophobic surfaces,” *Phys. Fluids*, **17**, 103606, (2005).

[37] J. Hou, B. Vajdi Hokmabad, and S. Ghaemi, “Three-dimensional measurement of turbulent flow over a riblet surface,” *Exp. Therm. Fluid Sci.*, **85**, 229–239, (2017).

[38] K. Fukagata, K. Iwamoto, and N. Kasagi, “Contribution of Reynolds stress distribution to the skin friction in wall-bounded flows,” *Phys. Fluids*, **14**, L73, (2002).